Journal of Biomedical Optics

BiomedicalOptics.SPIEDigitalLibrary.org

Intravascular optical coherence tomography to characterize tissue deformation during angioplasty: preliminary experiments with artery phantoms

Hamed Azarnoush
Sébastien Vergnole
Valérie Pazos
Charles-Étienne Bisaillon
Benoit Boulet
Guy Lamouche

SPIE.

Intravascular optical coherence tomography to characterize tissue deformation during angioplasty: preliminary experiments with artery phantoms

Hamed Azarnoush,[a,b,d] Sébastien Vergnole,[a,c] Valérie Pazos,[a] Charles-Étienne Bisaillon,[a] Benoit Boulet,[b] and Guy Lamouche[a]
[a]Institut des Matériaux Industriels, Conseil National de Recherches Canada, 75 de Mortagne, Boucherville, Quebec J4B 6Y4, Canada
[b]McGill University, Centre for Intelligent Machines, 3480 University, Montreal, Quebec, H3A 2A7, Canada
[c]Horiba Scientific, 231 rue de Lille, 59650 Villeneuve d'Ascq, France
[d]Montreal Neurological Hospital and Institute, 3801 University, Montreal, Quebec H3A 2B4, Canada

Abstract. We explored the potential of intravascular optical coherence tomography (IVOCT) to assess deformation during angioplasty balloon inflation. Using a semi-compliant balloon and artery phantoms, we considered two experimental scenarios. The goal for the first scenario was to investigate if variation in the elasticity of the structure surrounding the balloon could be sensed by IVOCT monitoring. In this scenario, we used three single-layer phantoms with various mechanical properties. Image analysis was performed to extract the inner and outer diameters of the phantoms at various pressures. The goal for the second scenario was twofold. First, we investigated the IVOCT capability to monitor a more complex balloon inflation process. The balloon was in a folded state prior to inflation. This allowed studying two stages of deformation: during balloon unfolding and during balloon expansion. Second, we investigated IVOCT capability to monitor the deformation in a three-layer phantom used to better mimic a true artery. So, not only were the IVOCT images processed to provide the inner and outer diameters of the phantom, but the layer thicknesses were also determined. In both scenarios, IVOCT monitoring revealed to be very efficient in providing relevant information about the phantom deformation during balloon inflation. © *2012 Society of Photo-Optical Instrumentation Engineers (SPIE).* [DOI: 10.1117/1.JBO.17.9.096015]

Keywords: angioplasty; optical coherence tomography; tissue characterization.

Paper 12051 received Jan. 24, 2012; revised manuscript received Jul. 22, 2012; accepted for publication Aug. 17, 2012; published online Sep. 18, 2012.

1 Introduction

Angioplasty is performed on over one million patients, every year, in the US alone.[1] It is the process of widening an artery where stenosis (narrowing of the lumen) has occurred due to presence of atherosclerotic plaque in vessel walls. Different interventional procedures are applied to provide the desired lumen patency. These procedures include inflation of a balloon or a stent where the narrowing has occurred. In earlier years, a large number of patients who were treated by angioplasty had to undergo repeated procedures, due to restenosis or recurrence of arterial narrowing.[2] Restenosis was correlated to the arterial injury, resulting from the excessive mechanical stretching of the vessel wall during balloon or stent deployment. The rate of restenosis was later reduced by using drug-eluting stents. This reduction was a result of adding a pharmacological contribution to the solution. Better results could still be obtained with the possibility to monitor the mechanical response of the arteries to prevent arterial damage during the intervention. Different methodologies have already been proposed for this purpose in the literature. Indeed, some researchers have proposed intravascular imaging of the vessel wall after angioplasty to verify the results. Among the proposed imaging modalities are intravascular ultrasound (IVUS)[3–5] and intravascular optical coherence tomography (IVOCT).[6–9] Both modalities provide cross-sectional images of the artery wall. IVUS provides a larger penetration depth, while IVOCT provides a better resolution. It has been shown that in comparison with IVUS, IVOCT provides a more accurate assessment of vessel wall layers,[7] stent deployment,[8] and plaque morphology.[9] The development of high-measurement rate swept-source optical coherence tomography (SS-OCT)[10] systems made IVOCT even more suitable for clinical application.

In this paper, we propose an application of IVOCT monitoring to characterize tissue deformation during angioplasty balloon inflation. Our assumption is that valuable information can be inferred from the measurement of deformation, leading, for example, to criteria that would insure a minimized risk of restenosis. Our intent is to propose a method to monitor deformation, a tool that could eventually be used in clinical investigations to identify, for example, the optimal conditions for balloon inflation.

In clinical practice, real-time intravascular imaging is not performed during balloon inflation. In order to visualize the artery, the operator deflates and withdraws the balloon catheter and replaces it with an imaging catheter to visualize the artery. In our setup, we use an integrated IVOCT imaging catheter to provide intravascular images during balloon inflation. Earlier, we proposed IVOCT monitoring[11] to characterize the deformation of angioplasty balloons. In the current work, we extend our

Address all correspondence to: Guy Lamouche, Institut des Matériaux Industriels, Conseil National de Recherches Canada, 75 de Mortagne, Boucherville, Quebec J4B 6Y4, Canada. Tel: 450-641-5198; Fax: 450-641-5106; E-mail: guy.lamouche@cnrc-nrc.gc.ca

0091-3286/2012/$25.00 © 2012 SPIE

previous work in using IVOCT monitoring to characterize the deformation of the structure surrounding the balloon. This is done with two experimental scenarios involving a semi-compliant balloon and artery phantoms.

In the first scenario, we fabricated three phantoms with different mechanical properties.[12] Then, we characterized the deformation of each phantom using IVOCT image analysis. The goal was to investigate if various mechanical properties of phantoms resulted in a relevant and measureable difference in image-based characterization of their deformation during inflation of an angioplasty balloon. Sensing variation of elasticity of phantoms becomes more challenging in the presence of the balloon which is made of a much stiffer material. Such investigation is potentially helpful in characterizing the elasticity of atherosclerotic arteries or distinguishing the composition of plaques, using balloon inflation monitoring results.

In the second scenario, we considered a case in which angioplasty was simulated more realistically to achieve two goals. The first goal was to investigate the effect of two regimes of the balloon inflation, i.e., the unfolding and the expansion, on the deformation of a phantom. This could provide insightful experimental information to improve the balloon folding methods and potentially reduce arterial damage during balloon unfolding. Previously, some authors have presented simulations[13,14] of the balloon unfolding process with the objective to improve stent deployment. To our knowledge, no experimental result on tissue characterization during balloon unfolding and inflation has yet been published. The second goal was to present how IVOCT image analysis could lead to a detailed assessment of the vessel wall structure, e.g., layer thickness characterization, during balloon inflation. Therefore, in the second scenario we used a phantom with several layers which simulated artery layers.

2 Materials and Methods

2.1 *Experimental Setup*

A custom-built SS-OCT system was used for imaging.[15] We used a wavelength-swept laser source (Santec, HSL2000) operating with a sweep rate of 30 kHz and a sweep range of over 110 nm around 1.31 μm wavelength to provide a measured axial resolution of about 12 μm in air. The catheter probe was designed to provide a spot size of 35 μm in diameter at a radial distance of about 2 mm in water. Imaging was performed at a rate of 20 frames per second leading to a transverse step of about 8 μm at a radial distance of 2 mm. The SS-OCT system was configured as a Mach-Zehnder interferometer with balanced detection and was packaged as a mobile unit.

Figure 1 illustrates the experimental setup for IVOCT monitoring of balloon inflation. In experiments, a polyurethane semi-compliant balloon with a nominal diameter of 4 mm was used. The IVOCT probe was composed of a single-mode

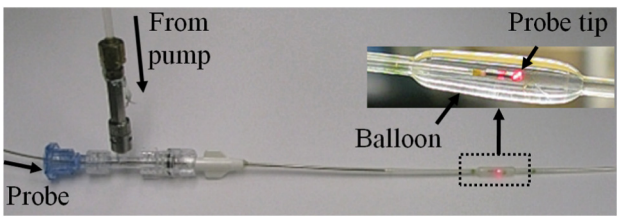

Fig. 1 Experimental setup, including the balloon, the probe, and the pump output.

fiber enclosed within a spiral metallic tube in the proximal region and within a polymer tube in the distal region. At the tip of the probe, light was focused by a gradient index (GRIN) lens and redirected at 90 deg by a right-angle prism. The IVOCT probe was inserted into the balloon catheter through a protective polymer sheath (PS). The PS was a tube which divided the lumen of the balloon catheter into two lumens, an outer high-pressure lumen for balloon inflation and an inner low-pressure lumen for the rotation of the probe. The balloon was inflated using pressurized water provided by a programmable syringe pump (PHD4400, Harvard Apparatus). The pressure was monitored by a pressure transducer and a pressure gauge at the output of the pump. As Fig. 1 illustrates, a T-connector connected the balloon catheter to the high-pressure line, allowing the IVOCT probe to be inserted in the balloon catheter. More details about the experimental setup have been presented previously.[11]

The phantoms used in this work were tubular structures fabricated with silicone using the method described in Ref. 12. To fabricate a layer, the material is deposited on a rotating shaft. The excess material is wiped with a blade which determines the thickness of a layer. The mixture is heated to accelerate polymerization. If many layers are required, they are deposited sequentially. The phantom is removed from the shaft at the end of the process. For each layer, the backscatter amplitude and the attenuation can be adjusted to replicate the optical behavior of true artery layers. This is achieved by introducing specific concentrations of alumina and carbon black in the silicone mixture. Mechanical properties can also be adjusted by varying the formulation of the silicone mixture.

2.2 *Experiments*

Two experimental scenarios were considered. In each experiment, we used the pump to inflate the balloon with incremental pressure steps. When the pressure was stabilized at each step, IVOCT monitoring was performed. A pressure range of 0 to 4 atm (atmosphere) was applied. In the following, we describe the details for each scenario.

2.2.1 *Scenario 1: monitoring the deformation of single-layer phantoms with different mechanical properties under balloon expansion*

For this experiment, we produced three phantoms with different mixture formulations.[12] Different formulations resulted in different mechanical properties, e.g., different degrees of elasticity. We characterized the elasticity of the phantoms before the monitoring experiments, using uniaxial tensile tests. During the fabrication of each phantom, a rectangular sample was produced from the same mixture, which was subjected to uniaxial tensile tests. The tensile tests provided stress-strain data showing a linear elastic behavior for each phantom material. Figure 2 presents these data for the three phantom materials (in dots with different colors on the online version). The Young's modulus (E) was obtained as the slope of the linear fit for each stress-strain curve. Young's modulus values of 1.07, 0.44, and 0.09 MPa were obtained for the three phantoms. These values are in a relevant range in comparison with real arteries.[16] In Fig. 2, these phantoms are identified as phantoms 1, 2, and 3, where phantom 1 is the stiffest phantom and phantom 3 is the softest phantom among the three phantoms. All phantoms used in this experiment were built in a single layer and had a nominal luminal

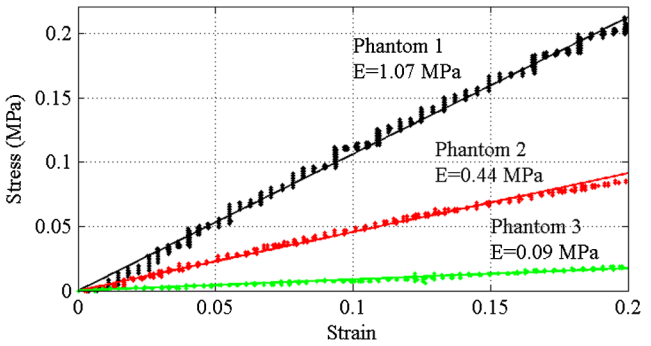

Fig. 2 Stress-strain data from uniaxial tensile tests with linear fits for phantoms 1,2, and 3; the phantoms being fabricated with different silicone formulations providing different mechanical properties.

diameter of 4 mm, which was equal to the nominal diameter of the balloon.

Figure 3(a) and 3(b) shows a sample IVOCT image, acquired in this experiment, in polar and Cartesian coordinates. The polymer sheath (PS), the balloon (B), and the phantom (P) are each represented by two contours, corresponding to their inner and outer surfaces. As the outer surface of the balloon overlapped the inner surface of the phantoms, these two surfaces are represented by a single contour. The contours C_{in} and C_{out} were detected to extract the inner and the outer diameters of the phantom at various pressures. The lowest contour in Fig. 3(a) and the innermost contour in Fig. 3(b), represent the prism surface (R). As will be explained later, the prism surface was used as a reference for image registration.

A sample A-scan, which is depicted by a red line in Fig. 3(a) and 3(b), is presented in Fig. 3(c). As the outer surface of the balloon overlapped the inner surface of the phantom, the balloon surfaces and the phantom surfaces appear as three spikes on the A-scan in Fig. 3(b). On most A-scans, the surfaces of the PS and the prism reveal themselves as spikes.

2.2.2 *Scenario 2: monitoring the deformation of a three-layer phantom under balloon unfolding followed by balloon expansion*

In this experiment, a more realistic and more complex case was considered, where the phantom had a nominal luminal diameter of 3.2 mm, which was smaller than the balloon's nominal diameter of 4 mm. In this case, the balloon was manually folded and inserted in the phantom. Therefore, the balloon was inflated starting in a folded state. The phantom deformation occurred in two regimes: first during the balloon unfolding and then during the balloon expansion. The balloon did not expand during unfolding, because the phantom was made of a material much softer than that of the balloon and in the unfolding stage only the phantom was expanded. The phantom had three layers that mimic the optical behavior of the intima, the media, and the adventitia of a porcine coronary artery.[12] For simplicity, these layers were made with the same mechanical properties in a range relevant to the properties provided in the literature.[16] A more complex phantom could be fabricated with different mechanical properties for each layer. Figure 4(a) and 4(b) shows a sample IVOCT image of a folded balloon inside the phantom in polar and Cartesian coordinates. In these figures, the artery phantom layers, namely, adventitia phantom (A), media phantom (M), and intima phantom (I) are identified. The contours C_A, C_M, and C_I were detected to extract diameter and thickness values at various pressures. The image was partially distorted, due to deflection of light in the balloon folding flap.

A sample A-scan, which is depicted by a red line, in Fig. 4(a) and 4(b) is presented in Fig. 4(c). The balloon surfaces corresponded to two spikes. The spike corresponding to the outer surface of the balloon overlapped the one corresponding to the intima phantom. Media and adventitia phantoms can be distinguished as regions with different intensity levels.

2.3 *Image Analysis*

In this subsection, we present the algorithms that were applied to extract contours which delimited phantoms or phantom layers. For each contour, one node per A-scan was detected. All algorithms were applied to image matrices in polar coordinates. The image intensity is denoted by I.

Images were registered in the radial direction to eliminate the variability of imaging depth. All images were registered by adjusting the radial optical distance with respect to the prism surface, which was located at a known distance from the axis of rotation of the probe. The prism surface (R) appeared as peaks on various A-scans. The radial position of these peaks was almost constant on these A-scans. Therefore, using a peak detection technique, one average radial value was detected to

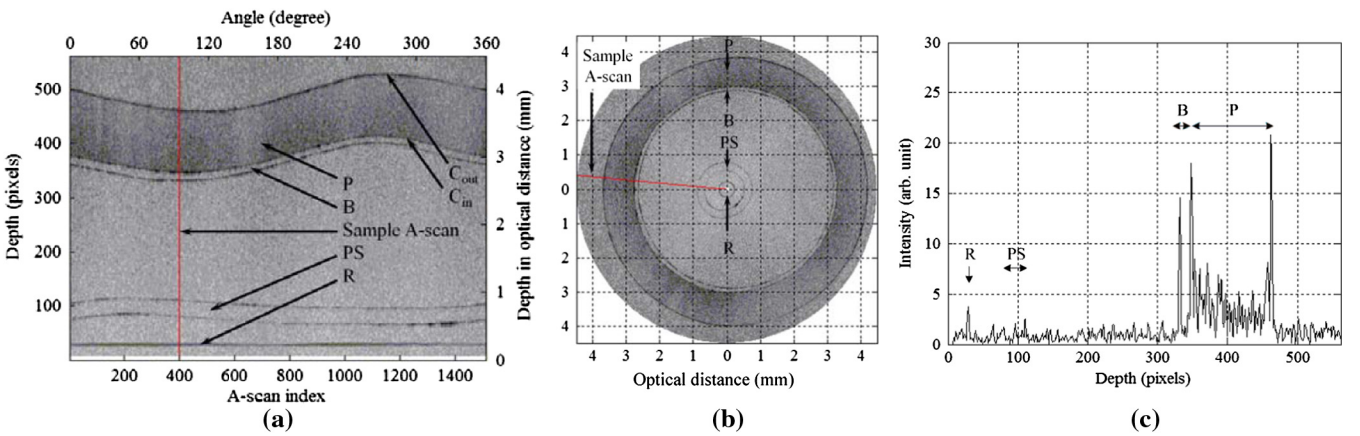

Fig. 3 Sample IVOCT image in (a) polar and (b) Cartesian coordinates, and (c) a sample A-scan from experiment 1 (B: balloon, C_{in}: inner phantom contour, C_{out}: outer phantom contour, P: phantom, PS: polymer sheath, and R: reference).

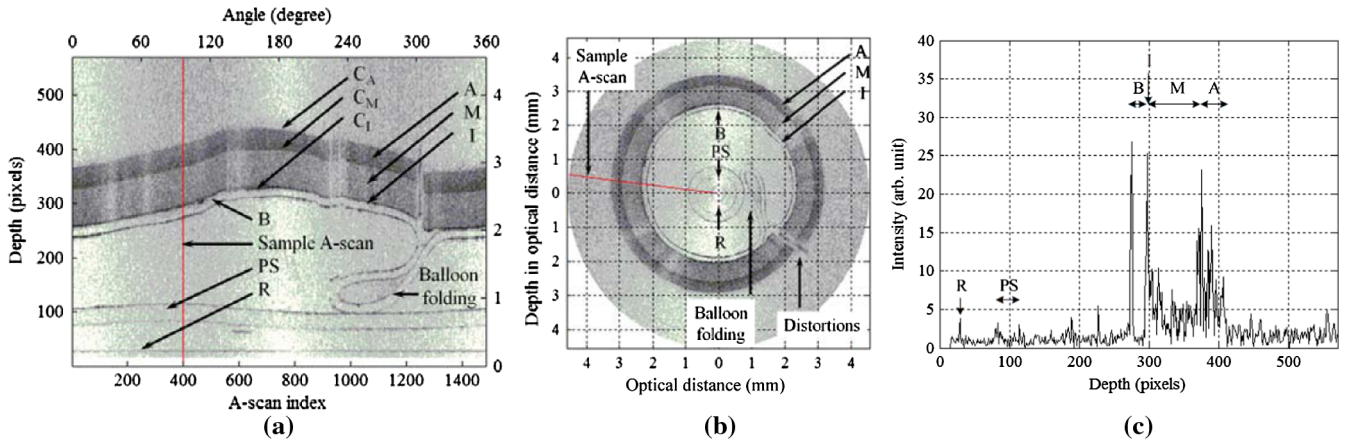

Fig. 4 Sample IVOCT image in (a) polar and (b) Cartesian coordinates, and (c) a sample A-scan from experiment 2 (B: balloon, *A*: adventitia, *I*: intima, *M*: media, C_A: adventitia contour, C_I: intima contour, C_M: media contour, PS: polymer sheath, and R: reference).

locate R on each image. The image I was then either cropped in radial direction or padded with rows of zeros to relocate the prism surface to the correct location. The padded regions are visible as white rectangles in Figs. 3(a) and 4(a).

In scenario 1, contours C_{in} and C_{out} were detected. These contours are identified in Fig. 3(a). In scenario 2, contours C_I, C_M, and C_A, were detected. These contours are identified in Fig. 4(a). One node per A-scan was detected. Each contour was classified as either a ridge[17] or an edge.[18]

2.3.1 *Scenario 1*

The contours C_{in} and C_{out} can be distinguished by spikes (local maxima) on most A-scans. These contours were detected as ridges. Let i_{in} and i_{out} denote nodes corresponding to the contours C_{in} and C_{out} on an arbitrary A-scan. In order to detect these nodes, first the A-scan was averaged with w neighboring A-scans on each side. The nodes i_{in} and i_{out} were obtained by searching for the local maxima.

2.3.2 *Scenario 2*

The contour C_I can be distinguished by spikes on various A-scans. This contour was detected as a ridge using a process similar to the one used to detect C_{in} in scenario 1. The contours C_M and C_A correspond to borders of regions with different intensity elevations. As the radial distance increases, C_M delineates a transition of lower intensity to higher intensity, while C_A delineates a transition from higher intensity to lower intensity. These contours were detected as edges using an edge template. Let i_I, i_M, and i_A denote nodes corresponding to the contours C_I, C_M, and C_A on an arbitrary A-scan. To locate the nodes i_M and i_A, the A-scan was convolved with an edge template. The template was a vector in the form of a step function, including "+1" elements corresponding to high intensities and "−1" elements corresponding to low intensities. The element on the step edge had a value of 0. The pixel that maximized the convolution of the A-scan with the template was detected as the edge pixel. The template used to detect i_M included a low-to-high step function and template used to detect i_A included a high-to-low step function.

2.4 *Estimation of Diameters from Contours*

In the image analysis algorithms, contour nodes were determined by pixel values. Pixel values were converted to depth values in millimeters in geometrical length.

In scenario 1, to obtain the depth value C_{in} node on a given A-scan, we used the equation:

$$r_{\text{in}} = r_R + s_{\text{axial}}\left(\frac{i_{\text{in}} - i_R}{n_w}\right), \tag{1}$$

where r_R is the distance of the prism surface from the center of rotation in millimeters in geometrical distance, s_{axial} is the pixel size in radial direction in optical distance, n_w is the refractive index for water, and r_{in} is the radial position of the C_{in} node in geometrical distance (in our conversions, $r_R = 0.15$ mm; $s_{\text{axial}} = 0.008$ mm, and $n_w = 1.33$).

To obtain the depth values for C_{out} node on a given A-scan, we used the equation:

$$r_{\text{out}} = r_R + s_{\text{axial}}\left(\frac{i_{\text{in}} - i_R}{n_w} + \frac{i_{\text{out}} - i_{\text{in}}}{n_p}\right), \tag{2}$$

where n_p was the refractive index for the phantom material, and r_{out} is the radial position of the C_{out} node in geometrical distance (in our conversions, $n_p = 1.41$). Positions of C_I nodes in geometrical distances were calculated similar to the calculation for C_{in} nodes using Eq. (1). Positions of C_M and C_A nodes in geometrical distances were calculated similar to the calculation for C_{out} nodes using Eq. (2).

3 Results

3.1 *Scenario 1*

In the IVOCT monitoring experiments, images were acquired during balloon inflation for pressures from 0 to 4 atm with 0.5 atm steps. Figure 5(a) and 5(b) shows examples of IVOCT images of the phantom 2 at pressures of 0 and 4 atm with the detected inner (C_{in}) and outer (C_{out}) surface contours (respectively, in blue and red on the online version). From the detected contours, average inner and outer diameters of the phantoms were calculated. Figure 6(a) presents these diameter values for different phantoms at different pressures. In the experiment involving phantom 3, the maximum applied pressure was 3.5 atm, because at higher pressures, some sections of the phantom were outside the IVOCT image range. As Fig. 6(a) shows, phantom 1 has the smallest and phantom 3 has the largest diameter growth rate. Therefore, considering the mechanical properties of the phantoms, IVOCT monitoring

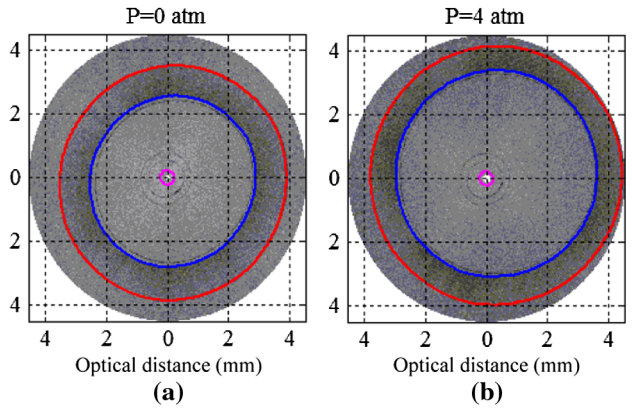

Fig. 5 Segmentation of IVOCT images of phantom 2 at pressures of (a) 0 atm and (b) 4 atm.

relevantly provides an indication of the elasticity of the surrounding structure. This means that one may be able to detect variation in elasticity, even in presence of a balloon which is made of a much stiffer material. Therefore, IVOCT monitoring during balloon inflation may also be used to characterize elasticity of arteries. Figure 6(b) presents the strain values obtained from IVOCT measurements. These include circumferential strain (ratio of increase in perimeter to original perimeter) and radial strain (ratio of increase in thickness to original thickness). We can see that strain values increase in magnitude when the phantom is softer. Radial strain values are negative since the phantom thickness decreases as a result of pressurization.

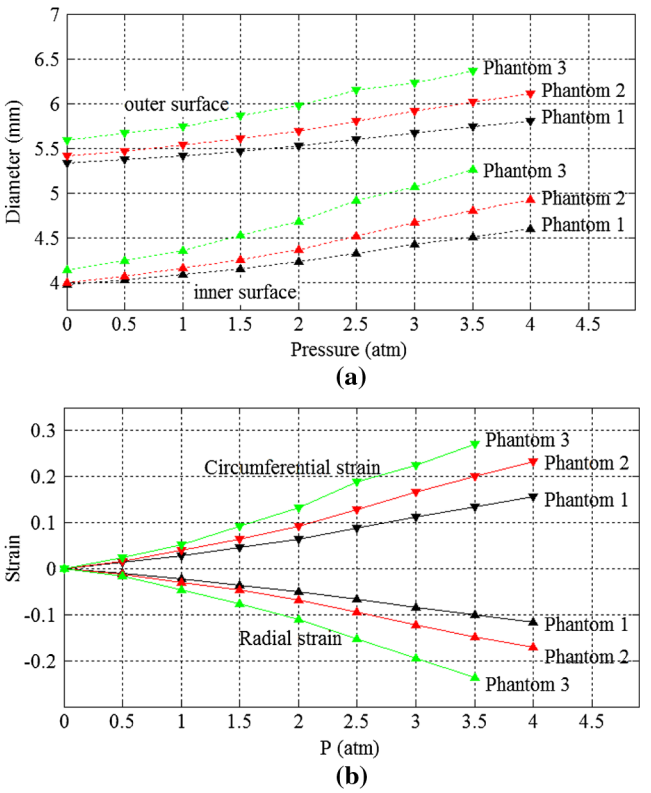

Fig. 6 (a) Comparison of inner and outer diameters obtained for the three phantoms from image analysis and (b) the resulting circumferential and radial strains.

3.2 *Scenario 2*

In this experiment, IVOCT images were acquired for pressures ranging from 0 to 4 atm with steps of 1 atm. Figure 7(a) illustrates the IVOCT image of the folded balloon inside the phantom at a pressure of 0 atm. Figure 7(b) presents the acquired image at pressure of 1 atm, where the balloon was partially unfolded. Figure 7(c) and 7(d) presents the acquired image at pressures of 2 and 4 atm, where the balloon was completely unfolded. In Fig. 7(a) and 7(d), the detected contours correspond to the inner surface of the phantom, media-adventitia interface, and the outer surface of the phantom (respectively, shown in blue, green, and red on the online version). These contours were used to measure diameter and thickness values. Figure 8 presents the calculated diameters. Based on IVOCT monitoring results in Fig. 8, the phantom underwent two phases of deformation with different rates. The first phase corresponded to pressures between 0 and 2 atm; the balloon was being unfolded. Therefore, it did not contribute to resistance against the pressurization resulting in a larger diameter growth rate for the phantom. The second phase corresponded to pressure values larger than 2 atm. In this phase, the balloon was completely unfolded. Therefore, further pressurization led to balloon expansion. Therefore, both the balloon and the phantom resisted the pressure, resulting in a smaller diameter growth rate for the phantom.

IVOCT cannot only monitor the variation of the inner and outer diameters of the phantom, but also of the variation of the layer thicknesses. Figure 9 demonstrates the values for the layer thicknesses averaged over all angles as a function of the inflation pressure. These are the thickness of the media, the thickness of the adventitia, and the total thickness of the phantom. The thickness of initima was too small to be

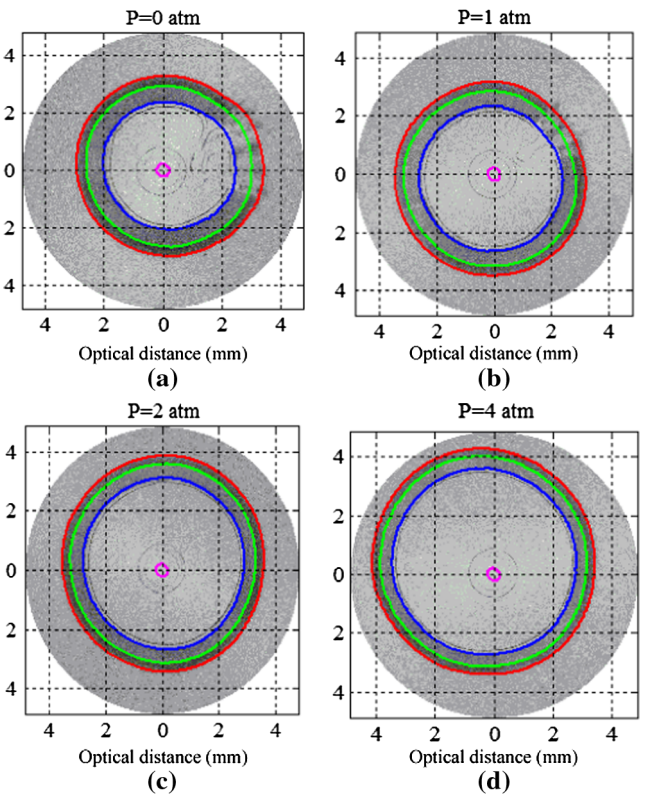

Fig. 7 Segmentation of IVOCT image of the phantom (a) and (b) during and (c) and (d) after the balloon unfolding process.

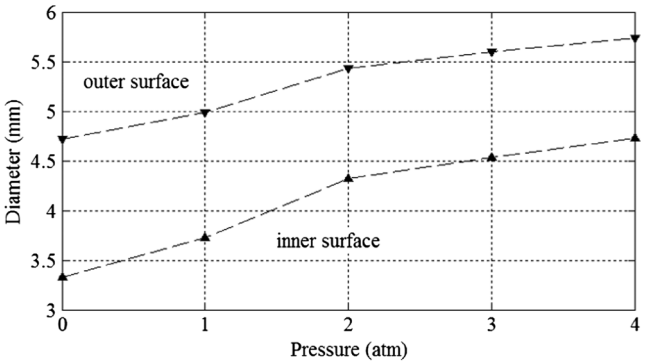

Fig. 8 Inner and outer diameters of the phantom during and after the balloon unfolding process.

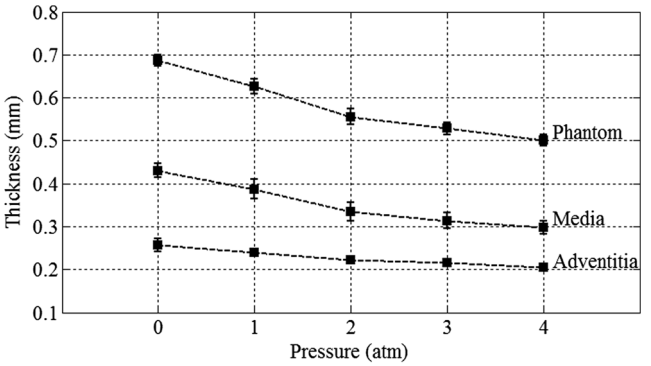

Fig. 9 Layer thickness characterization during the balloon unfolding and expansion at various pressures in steady state. The movie clip (Video 1) presents thickness characterization during continuous inflation (Video 1, MOV, 1.2 MB) [DOI: http://dx.doi.org/10.1117/1.JBO.17.9.096015.1].

calculated, given the axial resolution in the images. Using error bars, Fig. 9 also presents the standard deviation of the thicknesses over all angles. A similar two-phase trend can be distinguished in the layer thickness variation. The rate of decrease in the layer thicknesses is larger during the balloon unfolding process than it is during the balloon expansion process.

All the results presented so far, including the IVOCT images in Fig. 7, and the thickness characterization in Fig. 9, correspond to steady state, i.e., when the pressure was stabilized at each pressure step. Figure 9 also presents a movie clip where layer thickness characterization is performed during a continuous pressurization. This technique could potentially be useful to monitor the deformation of wall structure or the plaque in real-time for clinical or research purposes.

4 Discussion

4.1 *Scenario 1*

As can be seen in the results obtained from the uniaxial tensile tests (Fig. 2), the elastic modulus for the phantom materials differ significantly. This significant difference, however, is not appreciated between the results in Fig. 6. The reason is that these results represent the deformation for both the balloon and the phantom. Since the balloon material is much stiffer than the material for all phantoms, the difference between the phantom materials is less observable in IVOCT characterization results of Fig. 6. Nonetheless, IVOCT results are sufficiently accurate to distinguish different phantoms.

4.2 *Scenario 2*

In the current balloon folding configuration, depicted as a C-shape in Fig. 7(a), there was only one folded segment in the balloon. The balloon could also unfold starting with a different configuration, e.g., with multiple folds.[13] Regardless of the folding configuration, we expect to see a similar two-phase trend for the diameter and thickness values versus pressure measurements. In the first phase, there is at least one folded segment in the balloon that is unfolded and in the second phase, the unfolded balloon is expanded.

4.3 *Remaining Challenges*

This paper lays the foundation for OCT monitoring of the vessel response to balloon inflation. We thus set up two different scenarios, one involving vessels with different relevant mechanical properties and the other involving a vessel with multiple layers. For simplicity, we limited ourselves to experiments with artery phantoms. We also only characterized the vessel deformation. Natural extensions of this work are to perform such measurements on true arteries *in vivo* and to extract mechanical properties from the measured deformation.

Performing similar work on true arteries *in vivo* presents additional challenges, although all of them should be overcome. One challenge is that blood can degrade images acquired by IVOCT *in vivo*. Nevertheless, the only relevant imaging conditions are those were the balloon is close to or in contact with the artery wall. If only a thin layer of blood sits between the balloon exterior surface and the artery wall, the inner artery wall structures can still be observed,[15] allowing segmentation to be performed. In a recent work, we performed balloon inflation control in the near *in vivo* conditions provided by a beating heart setup.[19] Although the latter work did not involve segmentation of the artery wall structures, it showed that deformation monitoring can be done *in vivo* conditions. Another challenge is the integration of an IVOCT probe in percutaneous coronary intervention devices. Since IVOCT probes can be made quite small in diameter, i.e., a couple of hundred of micrometers, this is an engineering challenge that could easily be solved. Another challenge relates to the segmentation of artery wall structures. In the current paper, we used a phantom that mimics well defined artery layers. Layers in a true artery are not always easy to identify, especially for an atherosclerotic artery. We also decided to focus solely on layers for our preliminary study, nevertheless, other structures like plaque constituents could be monitored during the deformation. In our opinion, the segmentation of artery structures is the most significant challenge in bringing our proposed method to the clinical world, every specific case asking for a specific solution. Fortunately, there is currently active research in the identification of artery structures in IVOCT images to enhance the diagnostic capability of IVOCT. This should provide the tools needed to perform structure segmentation while monitoring the artery deformation.

In this paper, we focused on measuring deformations of phantoms with different elastic properties. Our method is not limited to linear elastic materials; it could be used to monitor the deformation of vessels which exhibit viscoelasticity. Measuring deformations already provides information that is relevant for diagnosis. More information could be obtained

by extracting mechanical properties using a constitutive model for the phantom material or vessel tissue. This could be done by developing optimization schemes to find the parameters that fit the mechanical model of the balloon-phantom system or the balloon-vessel system. This is a challenging task which is outside the scope of the current paper but that could provide added value to our proposed method.

5 Conclusion

The goal of this paper was to present IVOCT as a high-resolution imaging modality to characterize tissue deformation during angioplasty balloon inflation. Using image analysis techniques, we characterized the deformation of several phantoms in two scenarios. The implication of the first scenario was that variation in elasticity of tissues could be distinguished by image-based characterization even in presence of a balloon. The proposed technique could be helpful in cardiovascular research and in clinical applications. In further advanced applications, a mechanical analysis of the monitoring results could lead to an estimation of elasticity of arteries which could be performed during balloon angioplasty or balloon predilation in a stent implantation procedure. In the second scenario, we obtained a characterization of deformation during a balloon unfolding followed by an expansion process. In this scenario, a multilayer phantom was used. The layer thicknesses were also characterized during pressurization. By monitoring the layer thicknesses, we demonstrated that the shape of structures can be monitored during deformation. This could provide an insight into the composition of the vessel wall structure or the plaque in atherosclerotic arteries under balloon inflation. The evolution of the diameters and thicknesses also provided information on the effect of the unfolding and expansion process on tissue deformation.

Although we used phantoms, the proposed approach is not limited to phantoms. It could be used to study the response of arteries to different interventional procedures, applying different balloons, balloon folding methods, stents, or pressurization strategies. As a result, the proposed technique could be relevant to medical device industry, e.g., in improving balloon folding strategies, or in clinical applications, e.g., in improving pressurization strategies.

Acknowledgments

We acknowledge the financial support of the Genomics and Health Initiative of the National Research Council of Canada and the financial support of the Natural Sciences and Engineering Research Council of Canada.

References

1. D. Lloyd-Jones et al., "Heart disease and stroke statistics—2010 update: a report from the American Heart Association," *Circulation* **121**(7), e46–e215 (2010).
2. D. Faxon, *Restenosis: A Guide to Therapy*, Martin Dunitz, London (2001).
3. A. Colombo et al., "Intracoronary stenting without anticoagulation accomplished with intravascular ultrasound guidance," *Circulation* **91**(6), 1676–1688 (1995).
4. R. Blasini et al., "Comparison of angiography and intravascular ultrasound for the assessment of lumen size after coronary stent placement: impact of dilation pressures. Commentary," *Catheter. Cardiovas. Diag.* **42**(2), 113–120 (1997).
5. C. Briguori et al., "Discrepancy between angiography and intravascular ultrasound when analysing small coronary arteries," *Eur. Heart J.* **23**(3), 247–254 (2002).
6. E. Regar et al., *Optical Coherence Tomography in Cardiovascular Research*, Informa Healthcare, London (2007).
7. T. Kume et al., "Assessment of coronary intima-media thickness by optical coherence tomography: comparison with intravascular ultrasound," *Circulation* **69**(8), 903–907 (2005).
8. B. E. Bouma et al., "Interventional cardiology and surgery: evaluation of intracoronary stenting by intravascular optical coherence tomography," *Heart* **89**(3), 317–320 (2003).
9. I. K. Jang et al., "*In vivo* characterization of coronary atherosclerotic plaque by use of optical coherence tomography," *Circulation* **111**(12), 1551–1555 (2005).
10. G. J. Tearney et al., "Three-dimensional coronary artery microscopy by intracoronary optical frequency domain imaging," *J. Am. Coll. Cardiol.* **1**(6), 752–761 (2008).
11. H. Azarnoush et al., "Optical coherence tomography monitoring of angioplasty balloon inflation in a deployment tester," *Rev. Sci. Instrum.* **81**, 083101 (2010).
12. B. Charles-Étienne, M. L. Dufour, and G. Lamouche, "Artery phantoms for intravascular optical coherence tomography: healthy arteries," *Biomed. Opt. Express* **2**(9), 2599–2613 (2011).
13. A. J. Narracott et al., "Balloon folding affects the symmetry of stent deployment: experimental and computational evidence," in *Proc. of the 29th Int. Conf. of the IEEE Engineering in Medicine and Biology Society*, pp. 3069–3073, IEEE, Piscataway, NJ (2007).
14. M. De Beule et al., "Realistic finite element-based stent design: the impact of balloon folding," *J. Biomech.* **41**(2), 383–389 (2008).
15. G. Lamouche et al., "Intravascular optical coherence tomography on a beating heart model," *J. Biomed. Opt.* **15**(4), 046023 (2010).
16. G. A. Holzapfel et al., "Determination of layer-specific mechanical properties of human coronary arteries with nonatherosclerotic intimal thickening and related constitutive modeling," *Am. J. Physiol. Heart Circ. Physiol.* **289**(5), H2048–H2058 (2005).
17. D. Eberly, *Ridges in Image and Data Analysis*, Kluwer Academic Publishers, Dordrecht, The Netherlands (1996).
18. L. O'Gorman, M. J. Sammon, and M. Seul, *Practical Algorithms for Image Analysis: Description, Examples, Programs, and Projects*, Cambridge Univ. Press, Cambridge, United Kingdom (2008).
19. H. Azarnoush et al., "Real-time control of angioplasty balloon inflation based on feedback from intravascular optical coherence tomography: experimental validation using an excised heart and a beating heart model," *IEEE Trans. Biomed. Eng.* **59**(5), 1488–1495 (2012).